IEEE Access
Multidisciplinary | Rapid Review | Open Access Journal

Date of publication xxxx 00, 0000, date of current version xxxx 00, 0000.

Digital Object Identifier 10.1109/ACCESS.2024.1120000

A Novel Conical Cut Frequency-Tapered Ring Bar SWS for High-Power and Wide-Bandwidth K-Band TWTs

G. COMPARATO[1], G. PATERNA[1], G. LIPARI[1], E. TRAINA[2], A. MURATORE[1], A. BUSACCA[1], S. STIVALA[1], AND P. LIVRERI[1] (SENIOR MEMBER, IEEE)

[1]Department of Engineering, University of Palermo, 90128 Palermo, Italy
[2]Department of Engineering, University of Trento, 38122 Trento, Italy

Corresponding authors: G. Comparato (giorgia.comparato@unipa.it), P. Livreri (patrizia.livreri@unipa.it)

ABSTRACT This article presents a novel frequency-tapered Ring Bar Slow Wave Structure (RBSWS) for high-gain and wide-bandwidth Traveling Wave Tubes (TWTs) operating in the K-band for space applications. Starting from an analytical circuit model of the RBSWS, a conical-cut geometry is introduced to reduce the phase velocity. Our proposed novel RBSWS operates over a frequency range of 18.8 to 20.1 GHz, under a cathodic voltage and current of 19.8 kV and 0.3 A, respectively. Particle-In-Cell (PIC) results, carried out by CST Studio 2023, show a very high output peak power of 840.5 W at a gain of 20.2 dB, for an input power of 8 W, and an electron efficiency of 15.3%. The tapered RBSWS-TWT achieves a wider bandwidth, higher output power, and higher electron efficiency with respect to the untapered RBSWS-TWT, demonstrating the effectiveness of the proposed structure.

INDEX TERMS Millimeter-wave Power Amplifier, Ring Bar, Slow-Wave Structure, Traveling Wave Tubes, High power, Wide bandwidth.

I. INTRODUCTION

THE Ring Bar Slow Wave Structure (RBSWS) is becoming a key choice for the development of millimeter-wave high-power devices [1], [2], as the average power capability of the widely used circular helix is constrained by factors such as backward wave oscillation [3], [4], [5], [6] and heat dissipation [7], [8]. However, classical RBSWS is not always able to provide the desired output power owing its inherently limited bandwidth. In [9], square-ring vertex-bar (SRVB) and rectangular-ring vertex-bar (RRVB) Slow-Wave Structures (SWSs) have been proposed for the development of high-efficiency Traveling Wave Tubes (TWTs), showing a wider bandwidth compared to classical structures. A rectangular split resonant ring (RSRR) metamaterial absorber (MMA) was proposed to suppress backward wave oscillation (BWO) in a ring-bar traveling wave tube (RB-TWT). The RB-TWT with RSRR-MMA achieves a wider bandwidth and lower electron efficiency than the RB-TWT [10].

One of the major challenges associated with the design of TWTs is the degradation in performance caused by the interaction between the electron beam (EB) and the RF signal, which leads to a decrease in the average electron velocity [11], [12], [13], [14]. Several methodologies have been suggested to address this problem, notably, the integration of a tapered configuration at the end of the SWS [15], [16], [17] [18], [19]. To design a very high-efficiency, wide-bandwidth, and high output power TWT, a novel tapered ring-bar slow-wave structure was studied. Such a structure is a modified geometry of the contra-wound helix, known for its heightened gain and output power within a narrower bandwidth than the conventional helix [20], and its results were presented in [21]. In this study, starting from the analytical model reported in [22], the design of a frequency-tapered structure featuring a conical cut to broaden the bandwidth of the RBSWS through resynchronization of the electron beam, is presented. The results of this analysis provide valuable insights into TWT design and optimization, particularly those featuring RBSWS structures. The proposed frequency-tapering approach can enhance synchronization with an EB, which has given a portion of its energy, thereby improving the overall electrical performance. These findings have significant implications for the development of high-frequency devices that rely on the TWTs. The complete study of the novel proposed conical cut, starting from the analytical model, is discussed herein

and the results in terms of cold and hot-test parameters are reported. This article is organized as follows. In Section II, an analytical model of the equivalent circuit for the proposed novel structure is discussed. In Section III, the cold-test simulation results of the fundamental cell incorporating the novel proposed conical cut, carried out using CST Studio 2023, are provided. In Section IV, the hot-test parameters are reported. Finally, in Section V, conclusions are presented.

II. ANALYTICAL CIRCUIT MODEL FOR A RING BAR SWS

To obtain the dispersion diagram for the tapered circular ring bar SWS, an analytical model was implemented, starting from the equivalent circuit of the fundamental cell. In particular, the novel proposed conical cut is shown in the part marked in red in Fig. 1.

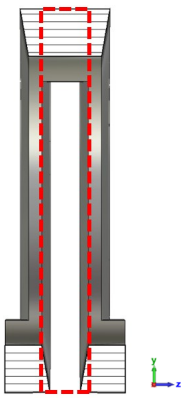

FIGURE 1. Fundamental cell of the RBSWS with the novel proposed conical cut.

The primary purpose was to determine the equivalent capacitance between the two rings and the inductance caused by the metallic bar between them, as highlighted in the blue section in Fig. 2.

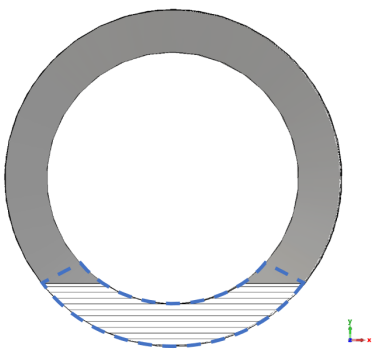

FIGURE 2. Front view of the SWS with a detail on the metallic bar between two consecutive rings.

It may be worthwhile to consider the capacitance that exists between the two parallel plane disks:

$$C = \frac{\varepsilon_0 \pi r^2}{d} \tag{1}$$

where ε_0 is the vacuum permittivity, d is the distance between the two adjacent disks, and r is the radius. Although this formula may serve as an initial approximation, it may not be sufficient for our scenario because we deal with two rings instead of disks. Therefore, adjustments were necessary. Furthermore, the formula may not fully account for fringing effects, which can be particularly significant when dealing with rings.

To approximate the capacitance of a ring-shaped capacitor, the following equation can be used:

$$C = \frac{\varepsilon_0 \pi (r_1^2 - r_2^2)}{d} \tag{2}$$

where r_1 and r_2 denote the outer and inner radii of the ring, respectively. The capacitance diminishes as the combined area of the two metal walls constituting the capacitor decreases. Notably, this equation has been found to provide a more precise estimation of capacitance than prior methodologies. Nonetheless, it is pertinent to acknowledge that the distance between the two walls of the capacitor may vary with radius. To obtain more accurate calculations, it is essential to consider the variability of this distance by defining it as a function of radius. This is achieved through a summation approach, as shown in (3), where the distance is iteratively calculated and incorporated into the overall capacitance estimation process. This careful consideration of the distance-radius relationship ensures robust results, enhancing the reliability of the capacitance calculations for the ring-shaped capacitor configuration. To address this task, we divided the surface of the rings into an equal number of n sections, each with an infinitesimal height h. Then, we calculated the capacitance of each of these individual rings. The cumulative capacitance was then determined by summing the capacitances of the individual rings as they operated in parallel.

$$C = \sum_{i=0}^{n} \frac{\varepsilon_0 \pi (r_{ext}^2(i) - r_{int}^2(i))}{d} \tag{3}$$

where $r_{ext}(i) = (r_2 + \Delta r) + i\Delta r = r_2 + (1 + i)\Delta r$ and $r_{int}(i) = r_2 + i\Delta r$ are the external and internal radii of the discretized segments, respectively, and $n = \frac{r_1 - r_2}{\Delta r}$ The maximum value that r_{ext} can reach is $r_1 = r_2 + n\Delta r$.

Fig. 3 illustrates the geometry that may be helpful in determining the equivalent circuit, where α is the cut angle, d_0 is the distance between the two rings when $\alpha = 0$, h is the height of the cut, and $\Delta d_i(r)$ is the infinitesimal d_0 increment depending on α and h is given by:

$$\Delta d_i(r) = h \tan \alpha = (r_1 - r_2) \tan \alpha \tag{4}$$

Starting from simulations, an optimum α value equal to 5° has been obtained.

Therefore, in general, considering the value of r between r_1 and r_2, we can write

$$d_i(r) = d_0 + 2\Delta d_i(r) = d_0 + 2(r_1 - \Delta r_i) \tan \alpha \tag{5}$$

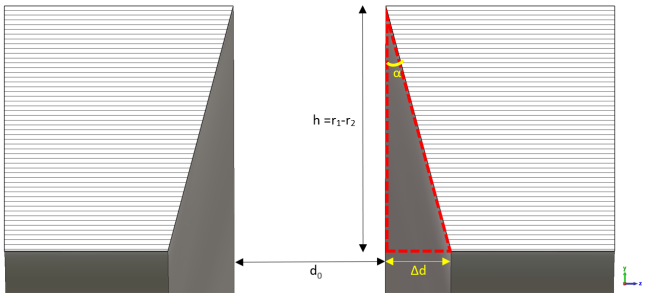

FIGURE 3. A geometric approach to solving radius-based calculations.

where Δr_i is the infinitesimal radius increment.
Then, (3) becomes

$$C = \sum_{i}^{n} \frac{\varepsilon_0 \pi (r_{ext}^2(i) - r_{int}^2(i))}{d_0 + 2(r_1 - \Delta r_i)\tan\alpha} \tag{6}$$

Similar to the effect of cuts, fringing effects need to be taken into account. These effects are crucial to consider for a structure such as this, and they become more significant in the presence of cuts. In the analytical model, the consideration of these effects could be a complex task, and some assumptions are necessary to simplify the model. The fringing effects in a capacitor composed of two parallel disks can be calculated using Sloggett's approach [23].

$$C_0 = C\left[1 + \frac{2d}{\pi R} ln\left(\frac{2e\pi R}{d}\right)\right] \tag{7}$$

where C_0 represents the capacitance of the capacitor when considering the fringing effects. In this context, d denotes the distance between the two disks and R is the inner radius of the waveguide, which is equal to 3.2 mm. The second term in the equation specifically accounts for the influence of the fringing effects along the outer edge of the capacitor plates. However, it is important to note the complexity of our configuration, as fringing effects manifest along both outer and inner edges.

We can adapt this formula to our case, so that we obtain C_0 as a function of (6), whereas for the second term of (7), we can write

$$C_0 = C\left\{1 + \left[\frac{2d(r_1)}{\pi r_1} ln\left(\frac{2e\pi r_1}{d(r_1)}\right)\right] + \left[\frac{2d(r_2)}{\pi r_2} ln\left(\frac{2e\pi r_2}{d(r_2)}\right)\right]\right\} \tag{8}$$

where the distances $d(r_1)$ and $d(r_2)$ are obtained by substituting $r = r_1$ and $r = r_2$ into (5), resulting in our case to C_0 equal to 2.08 pF.

This methodological approach serves to comprehensively address the intricacies associated not only with fringing effects along the outer and inner edges of the capacitor but also with the variable nature of the separation between the two capacitor plates. Significantly, this approach recognizes that the distance between the capacitor plates at the two edges is different, and exhibits a more generalized variation as a function of r. By systematically evaluating the distance at specific radii within the ring structure, we account for the relationship between the geometric configuration and the resulting electric field distribution. This consideration ensures a more accurate characterization of the capacitance of the ring-shaped capacitor, as it accurately captures the spatial variations in the distance and the corresponding influence on the capacitance. Thus, by incorporating these refined distance calculations into the capacitance estimation process, we achieved an exhaustive understanding of the behavior of the capacitor, increasing the reliability of our analysis. Equation (8) is a comprehensive formula that considers several factors, including the presence of the cut, the composition of the equivalent capacitance of two facing rings, and the variation in plate distance with radius. Additionally, it accounts for the fringing effects on both the outer and inner edges of the plates. It is strongly recommended that the blue element shown in Fig. 4 be ignored at this preliminary stage. However, it is important to consider that neglecting this element may potentially result in a reduction in the overall capacitance, as the effective area of the capacitor walls may be reduced. Notably, this aspect has not yet been considered. The aim is to determine the inductance introduced by the blue element. It is advisable to approach the problem in several stages, starting with an approximate case and then proceeding with more detailed considerations.

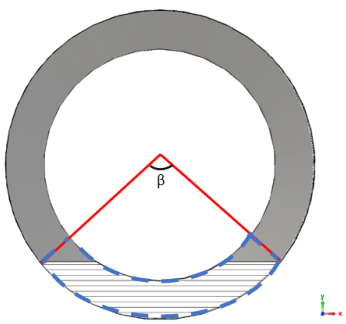

FIGURE 4. Estimation of inductance through circular sector calculation.

To represent the blue element, we can use a parallelepiped of length d, thickness $h = r_1 - r_2$, and width a. The width can be determined by measuring the length of both the inner and outer arches and calculating their averages. To estimate the value of the inductance associated with the bars numerically, we set the outer and inner arcs, a_1 and a_2, respectively, as

$$a_1 = 2.88 \text{ mm} \tag{9}$$

$$a_2 = 2.16 \text{ mm} \tag{10}$$

Hence, β results to be equal to:

$$\beta = \frac{a_1}{r_1} = \frac{2.88 \text{ mm}}{1.6 \text{ mm}} = 1.8 \text{ rad} \simeq 103.13^o$$

Using these two values, the mean value was calculated as $a = \frac{(a_1+a_2)}{2} = 2.52$ mm, which corresponds to the width of the equivalent parallelepiped. The formula for calculating the self-inductance of a rectangular-section wire is the well-known [24]:

$$L = 2 \cdot 10^{-3} d \left[ln\left(\frac{2d}{a+h}\right) + 0.5 + 0.2235\left(\frac{a+h}{d}\right)\right] = 0.0673 \text{ nH} \quad (11)$$

where $d = 0.25$ mm, $h = r_1 - r_2 = 0.4$ mm. It is recommended that the values in the formula be expressed in meters.

Taking into account the previous assumptions, it is possible to propose the equivalent circuit shown in Fig. 5.

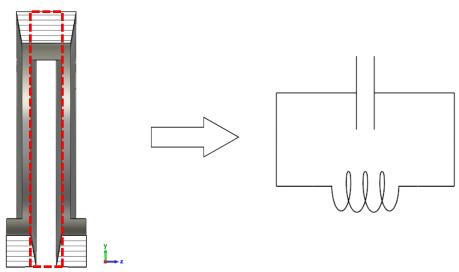

FIGURE 5. Equivalent circuit of the inner part of the novel proposed fundamental cell.

The resonant frequency of this LC circuit is given by the following equation:

$$f = \frac{1}{2\pi\sqrt{LC}} = 13.5 \text{ GHz} \quad (12)$$

Despite the numerous approximations made, the preliminary results align well with the simulation results, which will be discussed in the next section. Moving forward, we need to determine the capacitance $C_{tot,bar}$ between the SWS and the external waveguide, which involves breaking down the problem into several sub-problems. The first sub-problem is to determine the capacitance between the red surface shown in Fig. 6, that is, the metal piece connecting the two rings of the fundamental cell and the external waveguide.

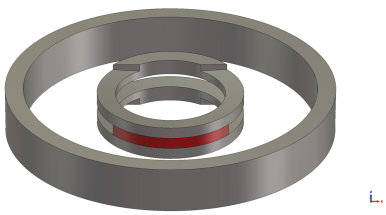

FIGURE 6. CST schematic model of a fundamental cell with a detail on the interface between the SWS and external waveguide.

The overall capacitance $C_{tot,bar}$ will be determined by the sum of two different contributions:

$$C_{tot,bar} = C_{0,ext} + C_{fringing} \quad (13)$$

where $C_{0,ext}$ is the capacitance between the metal piece connecting the two rings of the fundamental cell, and waveguide, as shown in Fig. 6, and $C_{fringing}$ is the capacitance resulting from the fringing effects. The first term can be obtained by using a method similar to that employed to derive the capacitance of a coaxial capacitor. It may be helpful to consider Gauss theorem for the electric field:

$$\oint_S \vec{E} \cdot \hat{n} dA = \frac{Q}{\varepsilon} \quad (14)$$

To determine the surface area of the red element, the length of circumference arc a_1 described in the previous equation can be calculated and then multiplied by the length along $\hat{z}$:

$$\oint_S \vec{E} \cdot \hat{n} dA = l\left(\frac{\beta}{360} 2\pi r\right)\vec{E} = \frac{Q}{\varepsilon_0} \quad (15)$$

The electric field can therefore be expressed as:

$$\vec{E} = \frac{Q}{\varepsilon_0}\frac{360}{\beta}\frac{1}{2\pi r l}\hat{r} \quad (16)$$

The aim was to calculate the voltage difference between the outer and inner conductors.

$$V = \int_{r_1}^{R} \vec{E} \cdot d\vec{l}_p = \frac{Q}{\varepsilon_0}\frac{360}{\beta}\frac{1}{2\pi l}\int_{r_1}^{R}\frac{1}{r}\hat{r} \cdot (\hat{r} dr) = = \frac{Q}{\varepsilon_0}\frac{360}{\beta}\frac{1}{2\pi l} ln\left(\frac{R}{r_1}\right) \quad (17)$$

where R is the inner radius of the waveguide.
And then the capacity can be calculated:

$$C_{0,ext} = \frac{Q}{V} = \varepsilon_0 \frac{\beta}{360}\frac{2\pi l}{ln\left(\frac{R}{r_1}\right)} = 6.62 \cdot 10^{-2} \text{ pF} \quad (18)$$

Calculating fringing capacity in this situation can be a complicated task. It is suggested to start by determining the electric field expressions along the x and y axes, as illustrated in Fig. 7, and then substituting them into (17).

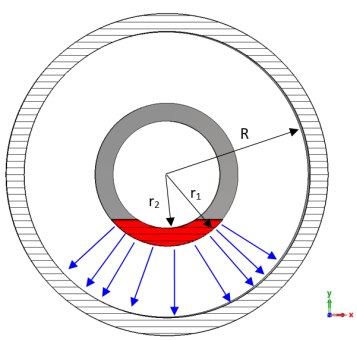

FIGURE 7. Representation of electric field lines.

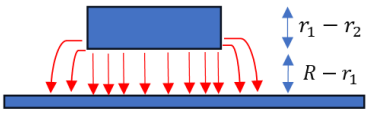

FIGURE 8. Simplified structure through a linearized circuit representation.

This structure is quite complex, but it is possible to represent a linearized version, as shown in Fig. 8.

The fringing capacity for this structure is known and is defined as:

$$C_{fringing} = \frac{2\pi\varepsilon_0}{log\left(\frac{R-r_1}{r_1-r_2}\right)} d_0 = 1.00 \cdot 10^{-2} \text{ pF} \qquad (19)$$

And so, the total capacity will be given by:

$$C_{tot,bar} = C_{0,ext} + C_{fringing} = \varepsilon_0 \frac{\beta}{360} \frac{2\pi l}{ln\left(\frac{R}{r_1}\right)} + \frac{2\pi\varepsilon_0}{log\left(\frac{R-r_1}{r_1-r_2}\right)} d_0 =$$

$$= 7.62 \cdot 10^{-2} \text{ pF} \qquad (20)$$

The inclusion of fringing effects in the capacitance model significantly improved the accuracy of our predictions. By considering these effects, we obtained a capacitance value which aligns well with theoretical expectations and experimental results. This adjustment ensures that our model accurately reflects the physical behavior of the capacitor, leading to more reliable performance metrics.

Then, it is necessary to determine the coupling capacities $C_{tot,rings}$ between the elements marked in blue in Fig. 9a and the waveguide.

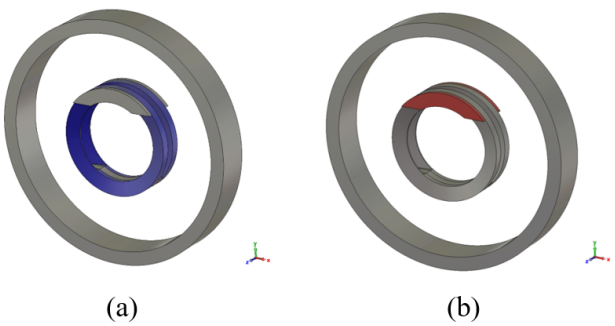

FIGURE 9. CST schematic model of a SWS with rings marked in blue used to calculate the coupling capacities between the SWS and waveguide (a), and bars marked in red used to calculate the associated capacitance and inductance (b).

$$C_{tot,rings} = C_{0,ext} \qquad (21)$$

Following an approach similar to that in (19), we can consider the capacitance resulting from the uniform distribution of the electric field. However, in this case, we do not have an arc of a circle but a complete circle; therefore, β is equal to 360°:

$$C_{tot,rings} = \frac{Q}{V} = 2\left[\varepsilon_0 \frac{2\pi l}{ln(\frac{R}{r_1})}\right] = 4.01 \cdot 10^{-2} \text{ pF} \qquad (22)$$

The reason for placing number 2 in front of the square brackets is that we consider two rings instead of one. Eventually, we need to derive the capacitance and inductance associated with the two elements in red illustrated in Fig. 9b, in which case the problem is solved using (11) and (20).

The equivalent circuit is illustrated in Fig. 10, and the parameter values are listed in Table 1.

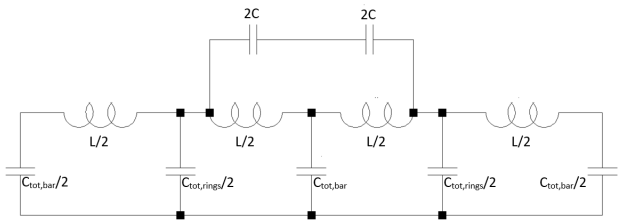

FIGURE 10. Final representation of the equivalent circuit.

TABLE 1. Values of equivalent circuit parameters.

Parameter	Value	Units
C	$2.08 \cdot 10^{-12}$	F
L	$6.73 \cdot 10^{-11}$	H
$C_{tot,bar}$	$7.62 \cdot 10^{-14}$	F
$C_{tot,rings}$	$4.01 \cdot 10^{-14}$	F

III. COLD-TEST PARAMETERS

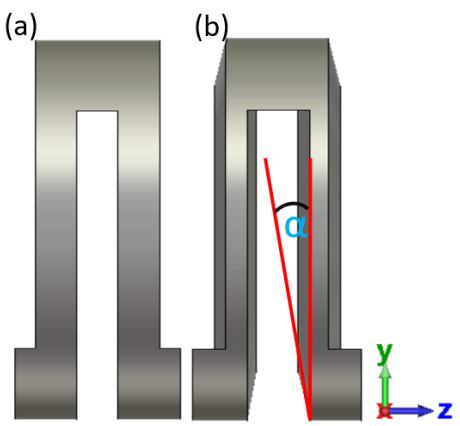

FIGURE 11. CST schematic model of the fundamental cell without (a) and with (b) the novel proposed conical cut.

Fig. 11 shows the fundamental cell of the RBSWS without (a) and with (b) the proposed conical cut. Owing to its introduction, the distance between the two rings of the fundamental cell becomes a function of the radius r and the cut angle α. Consequently, there is a reduction in the capacitive

effect between them, when α is positive, as depicted in the figure. The capacity between the two rings can be calculated using (6):

$$C_0 = \sum_{i}^{n} \frac{\varepsilon_0 \pi (r_1^2 - (r_2 + \Delta r_i)^2)}{d_0 + 2(r_1 - \Delta r_i)\tan\alpha}$$

A. EIGENMODE ANALYSIS

This type of simulation is used to determine the natural frequencies and corresponding propagation modes of a system by analyzing the fundamental cell of the structure [25]. The fundamental mode with the first two higher-order modes is depicted in Fig. 12, and Fig. 13 shows the phase velocity versus frequency for different α values. When α is equal to zero, the configuration returns to the classical RBSWS. When was greater than zero, there was a slight decrease in the phase velocity of the RF signal inside the fundamental cell.

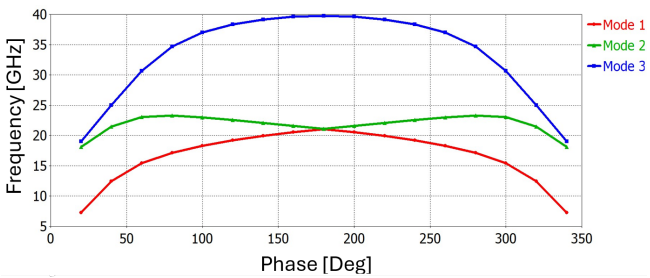

FIGURE 12. Categorizing mode frequencies: representation of the first three modes.

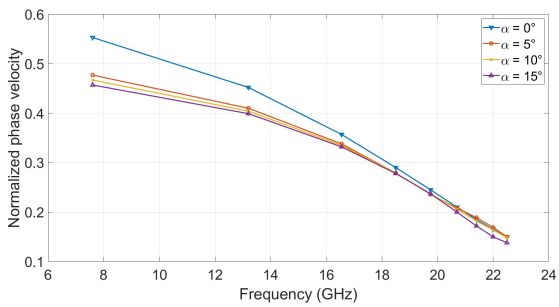

FIGURE 13. Normalized phase velocity versus frequency for different values of α.

1) Dispersion diagram

From the parameters previously determined using the analytical approach, MATLAB code was implemented to visualize the βL graph as a function of frequency. These results were then compared with eigenmode simulations obtained using CST. In the first analysis, the area occupied by the dielectric rods, which accounted for 20.45% of the total area, was considered. The reactance required for the calculation of the βL product was determined through the study of the ABCD matrix [26], [27] where C represents the susceptance:

$$\begin{bmatrix} V_1 \\ I_1 \end{bmatrix} = \begin{bmatrix} A & B \\ C & D \end{bmatrix} \begin{bmatrix} V_2 \\ -I_2 \end{bmatrix}$$

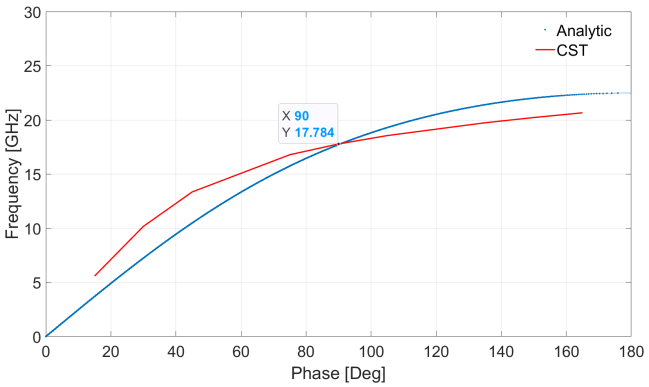

FIGURE 14. Dispersion diagram: Analytical model versus CST simulation.

Fig. 14 shows a comparison between the dispersion diagram obtained via the analytical model and that achieved by CST simulations. It can be observed that both the analytical and the CST simulation graphs show a frequency of approximately 17.7 GHz at the 90° phase.

B. S-PARAMETERS ANALYSIS

The S-parameters for the proposed structure were simulated using CST, and are shown in Fig. 15.

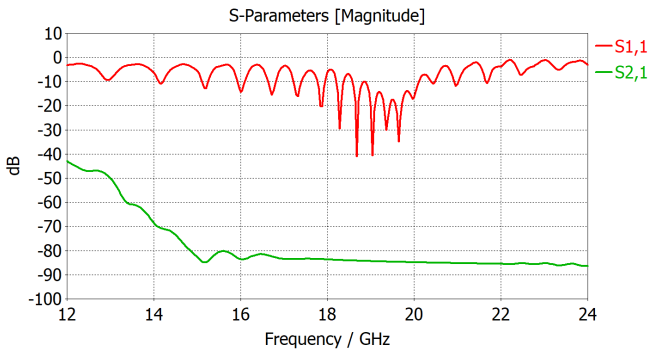

FIGURE 15. S-Parameters simulation using CST.

S_{11} parameter demonstrates a good matching over the K-band. The input-output isolation is provided by the sever, which provides an S_{21} of -80 dB in the matching band.

A schematic of the designed RBSWS with details of the last n fundamental cells of the second period with the novel proposed conical cut configuration is shown in Fig. 16.

To effectively separate the first section from the second section within the RBSWS, a high-loss section was introduced. This high-loss section was constructed using an AlN/SiC dielectric rod selected for its specific material properties, assuming a loss tangent ($\tan(\delta)$) of 0.28 and a dielectric constant of 21. The use of this dielectric material creates a

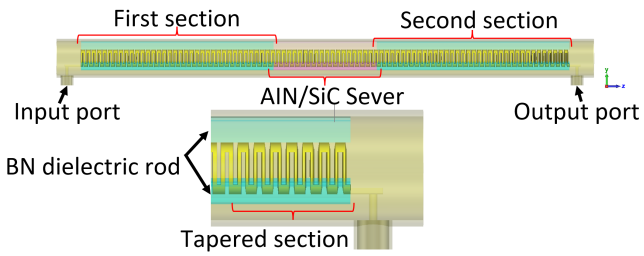

FIGURE 16. **CST schematic model of a two section RBSWS with the novel proposed conical cut tapered section.**

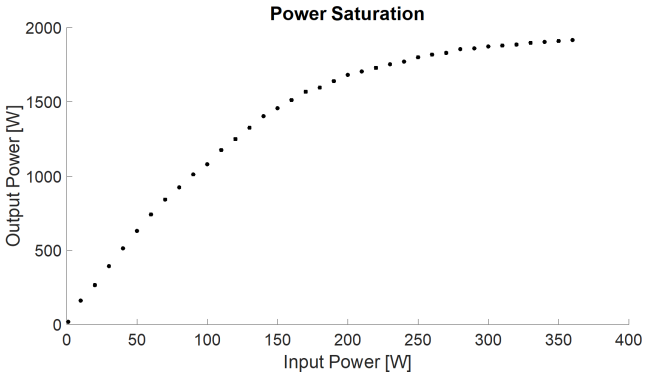

FIGURE 17. **Preliminary simulations: Power saturation.**

distinct boundary between the two sections of the RBSWS, allowing for efficient signal propagation while minimizing the unwanted interactions between them. In contrast, the dielectric material used in the remaining portion of the structure was Boron Nitride (BN), which was selected for its $\tan(\delta)$ and dielectric constant characteristics. With a significantly lower dissipation factor of 0.0009 and dielectric constant of 4.6, BN offers superior performance in maintaining signal integrity and minimizing signal loss within the structure. Coaxial cables with a characteristic impedance of 50 Ω were used to facilitate the input and output connections to the RBSWS. These cables provide impedance matching between the external components and RBSWS, optimizing the signal transfer efficiency and minimizing signal reflections.

IV. HOT-TEST PARAMETERS

Preliminary simulations were performed to investigate the power saturation and Fig.17 shows the power saturation graph [28]. In particular, power saturation was investigated in a single-section structure composed of 50 periods without taper, using an operating voltage of 19.8 kV, a current of 0.3 A, and a frequency of 19.4 GHz. The analysis was conducted by gradually increasing the input power and evaluating the output power response. Specifically, we monitored the output power as the input power was increased until the output power no longer increased linearly. The point at which the output power began to grow non-linearly was identified as the saturation value. It can be observed that the output power begins to saturate at an input power of approximately 250 W.

Starting from the results shown in the previous section, Particle-In-Cell (PIC) simulations were performed on a two-section RBSWS, each consisting of 50 periods using 54.014.512 meshcells. Moreover, boundary conditions such as Et = 0 have been considered in the edges and in the external surfaces of the waveguide, and an adiabatic system has been considered. To evaluate the performance of the RBSWS under operational conditions, PIC simulations were performed using CST Studio 2023 software, with an applied operating voltage of 19.8 kV and a current of 0.3 A. The electron beam within the structure was operated at a current density of 15 A/cm^2 and subjected to an analytic magnetic field of 0.5 T. The results of these simulations are shown in Fig. 18, which illustrates the relationship between the output power and frequency at varying values of the tapering parameter α, with the optimum value of tapered cells N_{cells} set at 7. For a given structure, saturation occurs when electrons lose synchronism with the phase velocity of the traveling wave. The optimum value of tapered cells was determined by varying the number of tapered cells and analyzing the resulting performance through simulations. Our simulations demonstrated that altering the number of tapered cells, either by increasing or decreasing, resulted in variations in the output power, specifically leading to a power decrease, as shown in Fig. 19. This graphical representation provides valuable insight into the performance characteristics of the RBSWS under different operating parameters, which helps optimize the device design and performance.

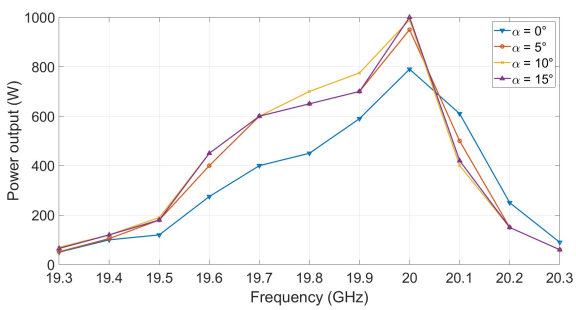

FIGURE 18. **Output power vs frequency for different values of α with $N_{cells} = 7$.**

When the input signal power is equal to 6 W, the structure without a taper presents a maximum output power of 790 W, whereas the tapered structure presents a maximum output power of 1 kW, with α equal to 10°. The introduction of the tapered section allows an increase in the output power by a factor of 25-35% in the frequency range between 18.8 and 20.1 GHz. The significant increase in output power observed with the tapered structure implies that, compared to the classic structure, achieving the same output power requires less input power, thereby reducing overall power consumption. As shown in Fig. 20, the PIC simulations were performed with an input power of 8 W, resulting in an output power of

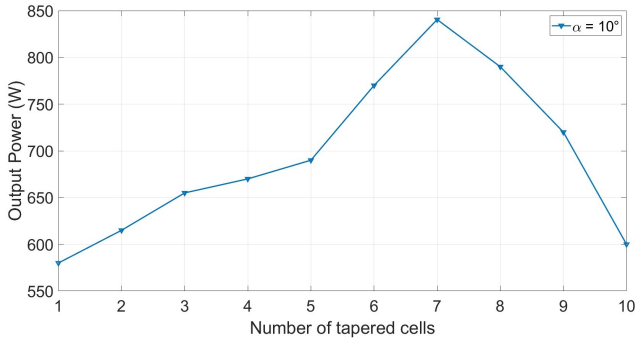

FIGURE 19. Output power for different values of tapered cells.

840.5 W. In Table 2, a comparison between the performance of the classical RBSWS and our novel proposed structure is presented, showing the effectiveness of our structure.

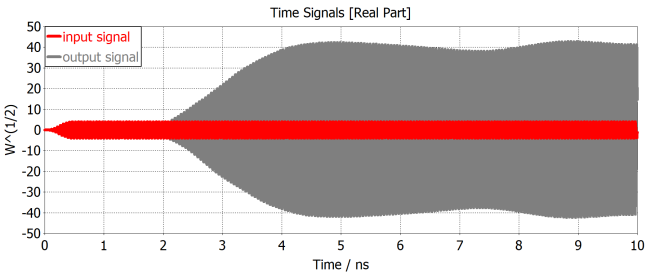

FIGURE 20. PIC simulation conducted on the two-section structure.

TABLE 2. Comparison between the novel structure and the classical SWS.

Performance	Classic RBSWS	Novel RBSWS	Units
Frequency Range	19.3-20.2	18.8-20.1	GHz
Cathodic Voltage	20.6	19.8	kV
Beam Current	0.3	0.3	A
Input Power	8	8	W
Output Peak Power	578	840.5	W
Gain	15.9	20.2	dB
Electron Efficiency	9.3	15.3	%

In Table 3, the performance comparison between our proposed conical cut configuration and state-of-art similar works, is presented.

TABLE 3. Comparison between our work and state-of-art similar works.

Performance	[This work] Conical Cut RBSWS	[9] Square-and Rectangular-Ring Vertex-Bar	[10] RSRR-MMA	Units
Frequency Range	18.8-20.1	28.5-35.5	9.1-12.7	GHz
Cathodic Voltage	19.8	15.7	27.5	kV
Beam Current	0.3	0.23	1.2	A
Peak Output Power	840.5	616 (Square), 695.6 (Rectangular)	5000	W
Electron Efficiency	15.3	17 (Square), 19 (Rectangular)	15	%

V. CONCLUSIONS

This article investigated the interaction of beam particles within a two-section RBSWS with a novel frequency-tapered section. The primary aim of the proposed conical cut was to reduce the equivalent capacitance between the two rings of the fundamental cell, resulting in a slight reduction in the phase velocity compared with the classical configurations. Particle-In-Cell (PIC) simulations, carried out using CST Studio 2023, show the effectiveness of integrating the tapered section with the proposed conical cut at the end of the slow-wave structure. The obtained results pave the way for developing a TWT based on the novel SWS, specifically designed for space applications. Before proceeding with the fabrication of the TWT based on the novel conical SWS, it is necessary to design all the essential parts of the amplifier for the physical realization of the TWT, specifically the electron gun [29], the collector, and the magnetic focusing system. We are currently developing an electron gun that employs scandium-doped cathodes. The use of scandium is crucial as it helps reduce the operating temperature, significantly enhancing the lifespan of the TWT. The structure of the electron gun is being meticulously designed to ensure optimal electron beam quality and stability. Lower operating temperatures achieved with scandium-doped cathodes are essential for efficient thermal management in the harsh space environment. Detailed simulations and preliminary tests are underway to optimize the electron gun design, focusing on beam convergence and minimizing beam spread. Regarding the collector, achieving an overall TWT efficiency higher than 50% is our primary goal. This efficiency target is critical for minimizing power consumption, which is a key consideration for space applications. The collector design is based on the electron efficiency obtained with the proposed interaction structure. To maximize energy recovery from the spent electron beam and enhance overall efficiency, we are designing a five-stage multistage collector (MSC), each stage coated with graphite. This coating is essential to minimize secondary electron emission, thereby increasing collector efficiency and stability. The design aims to recover as much energy as possible from the electron beam, reducing the thermal load on the collector. The focusing structure will employ a Periodic Permanent Magnet (PPM) configuration using samarium-cobalt magnets, chosen for their high residual magnetization. This selection ensures robust magnetic focusing, crucial for maintaining beam alignment and minimizing beam spread. We are exploiting a focusing structure, proposed by the same authors in [30], that promises to halve the weight of the focusing system. This innovative approach leverages advanced magnetic design techniques to reduce the system's weight without compromising performance, a critical consideration for space applications. The realization of the TWT with the novel conical SWS depends on the detailed design and optimization of the electron gun and collector. By employing scandium-doped cathodes, we aim to enhance the TWT's lifespan and reliability. The multistage collector, with its graphite coating and efficient energy recovery, is pivotal for achieving the desired efficiency. Additionally, the PPM

focusing structure, enhanced by our collaborative research on lightweight designs, will ensure robust beam focusing while minimizing the system's weight. We are committed to integrating these advanced design considerations into our TWT development to meet the stringent requirements of space applications. Detailed design studies and simulations are ongoing, and we will provide further updates as our research progresses.

REFERENCES

[1] J. H. Booske, R. J. Dobbs, C. D. Joye, C. L. Kory, G. R. Neil, G.-S. Park, J. Park, and R. J. Temkin, "Vacuum Electronic High Power Terahertz Sources," *IEEE Transactions on Terahertz Science and Technology*, vol. 1, no. 1, pp. 54–75, 2011.

[2] C. Paoloni, D. Gamzina, R. Letizia, Y. Zheng, and N. C. J. Luhmann, "Millimeter wave traveling wave tubes for the 21st century," *J. Electromagn. Waves Appl.*, vol. 35, no. 5, pp. 567–603, 2020.

[3] Y. L. Hu, Z. H. Yang, J. Q. Li, and B. Li, "Backward-Wave Oscillation Suppression in High-Power Broadband Helix Traveling-Wave Tubes," *IEEE Transactions on Electron Devices*, vol. 58, no. 5, pp. 1562–1569, 2011.

[4] M. Hägermann, P. Birtel, S. Meyne, D. Safi, and A. F. Jacob, "Magnetic Field Tapering Approaches for Backward-Wave Oscillation Suppression in Helix Traveling-Wave Tubes," *IEEE Transactions on Electron Devices*, vol. 65, no. 6, pp. 2236–2242, 2018.

[5] D. T. Lopes and C. C. Motta, "Characterization of ring-bar and contra-wound helix circuits for high-power traveling-wave tubes," *IEEE Trans. Electron Devices*, vol. 55, no. 9, p. 2498–2504, 2008.

[6] S. Sengele, M. L. Barsanti, T. A. Hargreaves, C. M. Armstrong, J. H. Booske, and L. Y. Y, "Backward-wave suppression analysis, and design and fabrication of a prototype millimeter-wave ringbar slow-wave structure," *IEEE Trans. Plasma Science*, vol. 42, no. 12, p. 3949–3960, 2008.

[7] P. Srikrishna, T. Chanakya, R. Venkateswaran, P. R. R. Rao, and S. K. Datta, "Thermal Analysis of High-Average Power Helix Traveling-Wave Tube," *IEEE Transactions on Electron Devices*, vol. 65, no. 6, pp. 2218–2226, 2018.

[8] J. Zhang, H. Yuan, Y. Wang, C. Shen, N. Bai, H. Fan, X. Zhao, J. Feng, and X. Sun, "Impact of Thermal State on Backward-Wave Oscillation in Helix TWT Under Operation," *IEEE Transactions on Electron Devices*, vol. 65, no. 6, pp. 2227–2235, 2018.

[9] W. Wei, S. Wang, Y. Wei, W. Hu, L. Zhang, Y. Dong, Z. Lu, Y. Jiang, and W. Wang, "Square- and Rectangular-Ring Vertex-Bar Slow Wave Structures for High-Efficiency Wide Bandwidth TWTs," *IEEE Transactions on Electron Devices*, vol. 70, no. 1, pp. 296–301, 2023.

[10] L. Yang, M. Ma, Y. Xie, H. Fan, Z. Chen, N. Bai, and X. Sun, "Investigation of High-Power Ring-Bar Traveling Wave Tube With Metamaterial Absorber," *IEEE Transactions on Plasma Science*, vol. 51, no. 2, pp. 392–398, 2023.

[11] A. S. Gilmour Jr, *Microwave and Millimeter-wave Vacuum Electron Devices*. Artech House, 2020.

[12] J. F. Gittins, *Power Traveling Wave Tubes*. American Elsevier Publishing Company, 1965.

[13] W. Gewartowski, *Principles Of Electron Tubes*. Van Nostrand, 1965.

[14] P. Livreri, "Design of a High-Efficiency Ka-Band TWT Power Amplifier for Radar Applications," *IEEE Transactions on Plasma Science*, vol. 50, pp. 2824–2829, Sept. 2022.

[15] N. H. Pond and R. J. Twiggs, "Improvement of traveling-wave tube efficiency through period tapering," *IEEE Transactions on Electron Devices*, vol. ED-13, pp. 956–961, Dec. 1966.

[16] T. K. Ghosh, A. J. Challis, A. Jacob, D. Bowler, and R. G. Carter, "Improvements in Performance of Broadband Helix Traveling-Wave Tubes," *IEEE Transactions on Electron Devices*, vol. 55, pp. 668–673, Feb. 2008.

[17] J. D. Wilson, "Design of high-efficiency wide-bandwidth coupled-cavity traveling-wave tube phase velocity tapers with simulated annealing algorithms," *IEEE Transactions on Electron Devices*, vol. 48, pp. 95–100, Jan. 2001.

[18] S.-S. Jung, A. V. Soukhov, B. Jia, and G.-S. Park, "Positive phase-velocity tapering of broadband helix traveling-wave tubes for efficiency enhancement," *Appl. Phys. Lett.*, vol. 80, pp. 3000–3002, April 2002.

[19] Y. N. Pchelnikov, "Ring-Double-Bar Slow Wave Structure for High Power TWTs," *IEEE Transactions on Electron Devices*, vol. 63, pp. 4479–4483, Nov. 2016.

[20] C. Chua, A. Sheel, T. Julius, T. Mush, and Shen, "Microfabricated planar helical slow-wave structures based on straight-edge connections for THz vacuum electron devices," *Terahertz Science and Technology*, vol. 4, pp. 208–229, 2011.

[21] G. Comparato, G. Paterna, G. Lipari, E. Traina, A. Muratore, A. Busacca, S. Stivala, and P. Livreri, "Design of a Novel Conical Cut Frequency-Taper for a K-band Ring Bar Slow Wave Structure," in *2024 IEEE IVEC Conference*, (Monterey, CA), April 2024.

[22] S. K. Datta, V. B. Naidu, P. R. R. Rao, L. Kumar, and B. Basu, "Equivalent Circuit Analysis of a Ring–Bar Slow-Wave Structure for High-Power Traveling-Wave Tubes," *IEEE Transactions on Electron Devices*, vol. 56, no. 12, pp. 3184–3190, 2009.

[23] G. J. Sloggett, N. G. Barton, and S. J. Spencer, "Fringing fields in disc capacitors," *Journal of Physics A: Mathematical and General*, vol. 19, no. 14, pp. 2725–2736, 1986.

[24] *Radio Engineers Handbook*. New York: McGraw-Hill, 1945.

[25] G. Paterna, G. Lipari, E. Traina, G. Comparato, A. Muratore, P. Livreri, S. Stivala, and A. Busacca, "Design of a Low Voltage and High Power Traveling Wave Tube Based on a Sheet-Beam Rectangular Ring-Bar Slow-Wave Structure," *IEEE Access*, vol. 12, pp. 9062–9069, 2024.

[26] R. Collin, *Foundations for Microwave Engineering, 2nd Ed.* McGraw-Hill series in electrical engineering: Radar and antennas, Wiley India Pvt. Limited, 2007.

[27] K. Rouhi, R. Marosi, T. Mealy, A. Figotin, and F. Capolino, "Parametric Modeling of Serpentine Waveguide Traveling Wave Tubes," *IEEE Transactions on Plasma Science*, pp. 1–17, 2024.

[28] D. Gong, T. Huang, J. Li, and B. Li, "Research on Automatic Measurement Method of Saturation Characteristics of Broadband TWT," in *2019 International Vacuum Electronics Conference (IVEC)*, (Busan, Korea (South)), pp. 1–2, 2019.

[29] P. Livreri, R. Badalamenti, and A. Muratore, "Optimum Design and Performance of an Electron Gun for a Ka-Band TWT," *IEEE Transactions on Electron Devices*, vol. 66, no. 9, pp. 4036–4041, 2019.

[30] G. Paterna, G. Comparato, G. Lipari, E. Traina, A. Muratore, A. Busacca, P. Livreri, and S. Stivala, "Comparison between Halbach Array and Periodic Permanent Magnet Circuit configuration," in *2024 IEEE IVEC Conference*, (Monterey, CA), April 2024.

G. COMPARATO received the bachelor's degree in Cybernetics Engineering from the University of Palermo, in 2022. Since 2022, she is a student of the Master's course in Electronics Engineering at the University of Palermo, Italy. She is currently working on her master's degree thesis focused on Ring Bar SWSs. Her research interests include TWTs for space applications.

G. PATERNA received the B.S. and M.S. degrees in electronics engineering from the University of Palermo, Italy, in 2020 and 2023, respectively. He is currently a PhD student in Information and Communication Technologies at the University of Palermo, IT. His research interests include microwave vacuum electron tubes, mostly on High power microwave devices, slow-wave structures, electron guns, and microwave devices.

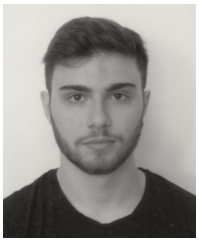

G. LIPARI received the B.S. and M.S. degrees in electronics engineering from the University of Palermo, Italy, in 2020 and 2023, respectively. He is currently a PhD student in Information and Communication Technologies at the University of Palermo, IT. His research interests include microwave vacuum electron tubes, mostly on TWTs for space applications, slow-wave structures, electron guns, and microwave devices.

E. TRAINA received the B.S. and M.S. degrees in electronics engineering from the University of Palermo, Italy, in 2020 and 2023, respectively. She is currently a PhD student in Space science and technology at the University of Trento, IT. Her research interests include vacuum electron tubes, mostly on Extended interaction Klystrons, microwave slow-wave structures, electron guns, and microwave devices.

A. MURATORE is a senior designer and a lecturer for the Microwave electronics course at the Department of Engineering of the University of Palermo, Italy, since 2020. He received his master's degree in electronic engineering in 1973. He has a background of more than 30 years working in Vacuum Electronics with Leonardo Company covering also the position of manager.

A. BUSACCA is Full Professor of Electronics at the Department of Engineering of the University of Palermo, Italy, since September 2018. He received the master's degree in electronic engineering and the Ph.D. Degree in Electronic, Computer and Telecommunication Engineering from the University of Palermo in 1998 and 2002, respectively. He was also involved as a WP leader or Coordinator in several projects financed from private industries, the Italian Ministry of University and Research, the Italian and the European Space Agency, the European Community. His main research interests include: power electronics, power converters, characterization of SiC and GaN devices for automotive applications, LIDAR and sensors for autonomous drive, photodetectors characterization, photonic microtechnologies, optical fibre devices, linear and nonlinear integrated optical devices, optoelectronic devices, design and realization of multisensor wearable devices for biomedical applications, free space optics communication, fabrication and characterization of photovoltaic cells, TeraHertz science. Prof. Busacca is author or co-author of more than 200 publications on prestigious International Journals and Conferences.

S. STIVALA is Associate Professor of Electronics at the Department of Engineering of the University of Palermo (UNIPA - Italy), since July 2020. He received the master's degree in electronic engineering and the Ph.D. Degree in Electronic and Telecommunication Engineering from the University of Palermo in 2004 and 2008, respectively. He is the Coordinator for the Master's degree programs in Electronics Engineering (since December 2022) and Member of the PhD board in "Information and Communication Technologies". His main research interests include: design and characterization on RF/microwave devices and circuits, TeraHertz spectroscopy, optical and electrical characterization of photodetectors, optoelectronic devices, biophotonics and error mitigation in free-space optical communications. Prof. Stivala is author or co-author of about 100 publications on prestigious International Journals and Conferences.

P. LIVRERI (IEEE Senior Member) received the Laurea degree (Hons.) in electronics engineering, and the Ph.D. degree in electronics and communications engineering from the University of Palermo, Italy, in 1986 and 1992, respectively. From 1993 to 1994, she was a Researcher with the National Council for Researches, CNR, Rome, Italy. Since 1995, she has been serving as the Scientific Director for the Microwave Instruments and Measurements Laboratory with the Department of Engineering, University of Palermo. In 2020, she also joined the CNIT National Laboratory for Radar and Surveillance Systems RaSS, Pisa. She is currently a Professor with the Department of Engineering, University of Palermo, and a Visiting Professor with the San Diego State University. She is a Principal Investigator of the "Microwave Quantum Radar" project, funded by the Ministry of Defense, in 2021. Her research interests include microwave and millimeter wave vacuum high power amplifier (TWT, Klystron) and solid-state power amplifiers for radar applications; high power microwave sources (virtual cathode oscillator and magnetically insulated transmission line oscillator); microwave and optical antennas; radar; and microwave quantum radar. Prof. Livreri is author or co-author of more than 200 publications on prestigious International Journals and Conferences. She also serves as an Associate Editor for IEEE ACCESS.